



# Novel visible-light-driven Z-scheme $\text{Bi}_{12}\text{GeO}_{20}/\text{g-C}_3\text{N}_4$ photocatalyst: Oxygen-induced pathway of organic pollutants degradation and proton assisted electron transfer mechanism of Cr(VI) reduction



Zhen Wan <sup>a,b</sup>, Gaoke Zhang <sup>a,\*</sup>, Xiaoyong Wu <sup>a</sup>, Shu Yin <sup>c,\*</sup>

<sup>a</sup> Hubei Key Laboratory of Mineral Resources Processing and Environment, School of Resources and Environmental Engineering, Wuhan University of Technology, Wuhan 430070, China

<sup>b</sup> Key Laboratory of Photochemistry, Beijing National Laboratory for Molecular Sciences, Institute of Chemistry, Chinese Academy of Sciences, Beijing 100190, China

<sup>c</sup> Institute of Multidisciplinary Research for Advanced Materials, Tohoku University, 2-1-1, Katahira, Aoba-ku, Sendai 980-8577, Japan

## ARTICLE INFO

### Article history:

Received 10 December 2016

Received in revised form 2 February 2017

Accepted 5 February 2017

Available online 6 February 2017

### Keywords:

Z-scheme

$\text{Bi}_{12}\text{GeO}_{20}/\text{g-C}_3\text{N}_4$  composite

Oxygen-induced pathway

Kinetic isotope effect

Proton assisted electron transfer

## ABSTRACT

We successfully synthesized novel solid state Z-scheme visible-light-driven  $\text{Bi}_{12}\text{GeO}_{20}/\text{g-C}_3\text{N}_4$  composite photocatalysts and investigated their photocatalytic activities for degradation of microcystin-LR and RhB, and for reduction of aqueous Cr(VI). The TEM and HRTEM images clearly showed the heterogeneous nanostructures at the interface between  $\text{Bi}_{12}\text{GeO}_{20}$  and  $\text{g-C}_3\text{N}_4$ . The as-prepared  $\text{Bi}_{12}\text{GeO}_{20}/\text{g-C}_3\text{N}_4$  composites exhibited enhanced photocatalytic activities for the degradation of microcystin-LR and RhB aqueous solution and reduction of aqueous Cr(VI) as compared to the pure  $\text{Bi}_{12}\text{GeO}_{20}$  and  $\text{g-C}_3\text{N}_4$  under visible-light irradiation. On the basis of the radical species trapping experiments and ESR analyses,  $\text{O}_2^{\cdot-}$  and  $\text{h}^+$  were confirmed to be the mainly active species involved in the degradation of organic pollutants and this reaction was identified to be an oxygen-induced pathway. Meanwhile, combined with the in situ ATR-FTIR spectroscopy and kinetic isotope effect investigations, the photocatalytic reduction of aqueous Cr(VI) was identified as a proton assisted electron transfer reaction. Moreover, the enhanced photocatalytic activities of the  $\text{Bi}_{12}\text{GeO}_{20}/\text{g-C}_3\text{N}_4$  composites can be attributed to the improved photo-absorption properties and effective separation of photo-induced charge carriers caused by the Z-scheme system of the as-prepared  $\text{Bi}_{12}\text{GeO}_{20}/\text{g-C}_3\text{N}_4$  composites.

© 2017 Elsevier B.V. All rights reserved.

## 1. Introduction

Semiconductor photocatalysis has attracted wide attentions due to its wide applications in resolving environmental problems caused by hazardous pollutants [1–5]. Among them, Bi-based photocatalysts are suggested to be the viable photocatalysts and have been widely investigated [6,7]. In the previous reports, bismuth germanate ( $\text{Bi}_{12}\text{GeO}_{20}$ , Fig. 1b), with a lattice constant of 10.013 Å and a total of 66 atoms in a supercell, belongs to the sillenite group of cubic crystals of the I23 space group, and exhibited strong oxidizing power for the photocatalytic degradation of various contaminations irrespective of pollutions in water or air [8,9]. However, despite it fits the essential demand for an effective photocatalyst, the high recombination of photo-induced carriers and poor visible-light responsiveness limit its further applications

in environmental protection area [10]. Consequently, it is necessary to take effective strategies to suppress the recombination of photo-induced electrons and holes.

In a general way, construction of the heterogeneous semiconductors has been found to be an effective approach. Fang et al. reported that the  $\text{Ag}_3\text{PO}_4/\text{AgI}$  photocatalysts exhibited better photocatalytic activities than single-phase  $\text{Ag}_3\text{PO}_4$  or  $\text{AgI}$  due to the enhanced separation efficiency [11]. Wang et al. synthesized the *p-n* junction  $\text{Cu}_2\text{O}/\text{BiVO}_4$  heterogeneous nanostructures which exhibited much higher visible-light photocatalytic activities than the individual  $\text{BiVO}_4$  nanocrystals for the degradation of methylene blue and phenol [12]. However, in spite of the higher separation efficiency, the transferred photo-induced carriers exhibited lower oxidation and reduction abilities than original electrons and holes in this way. To solve this problem, novel Z-scheme photocatalysts have become a hot topic because of their enhanced separation efficiencies and undiminished photo-oxidation or photo-reduction performances. For example, Z-scheme  $\text{g-C}_3\text{N}_4\text{-WO}_3$  exhibited enhanced photocatalytic activities than single-phase photocatalyst for the degradation of methylene blue and fuchsin [13].

\* Corresponding authors.

E-mail addresses: [gkzhang@whut.edu.cn](mailto:gkzhang@whut.edu.cn) (G. Zhang), [\(S. Yin\).](mailto:shuyin@tagen.tohoku.ac.jp)

$\text{V}_2\text{O}_5/\text{g-C}_3\text{N}_4$  Z-scheme photocatalysts prolonged the lifetime of photo-induced carriers, and increased the photocatalyst activities [14].

Recently, a novel metal-free semiconductor, graphite-like carbon nitride ( $\text{g-C}_3\text{N}_4$ ), has been intensely studied as a material for electrochemical electrode, photocatalyst and gas sensors [15–20]. Its abundant raw materials and nontoxicity are preferable features for large-scale production and applications. Owing to the  $\text{sp}^2$  hybridization of carbon and nitrogen atoms forming  $\pi$ -conjugated graphitic planes, it exhibits strong photoconductivity (high discharge and charge current rates), good stability and visible-light responsiveness (~2.7 eV) [21]. Wang et al. synthesized B-modified  $\text{g-C}_3\text{N}_4$  nanosheets by a thermal-induced polymerization of urea and  $\text{Ph}_4\text{BNa}$  in a one-pot fashion. The prepared sample showed a much higher hydrogen evolution activity than that of the pure urea-derived  $\text{g-C}_3\text{N}_4$  catalyst [22]. Wang et al. also reported the direct splitting of pure water by modified  $\text{g-C}_3\text{N}_4$  with Pt,  $\text{PtO}_x$ , and  $\text{CoO}_x$  as redox cocatalysts [23]. Therefore, coupling the semiconductor photocatalyst with  $\text{g-C}_3\text{N}_4$  to form a Z-scheme photocatalytic system is a promising strategy to improve its photocatalytic activities. As for the unique properties of the  $\text{g-C}_3\text{N}_4$ , it can improve not only the absorption of visible-light, but also the separation and transport of photo-induced carriers [24,25].

Nowadays, numerous works have been made to explore the fundamental mechanism of the photocatalytic reactions [26–28]. Traditionally, these reactions are usually discussed in terms of interfacial single electron transfer followed by free-radical ion or free-radical active species such as the  $\cdot\text{OH}$ ,  $\text{O}_2^{\bullet-}$  and  $\text{h}^+$  [26]. Specifically, in these reactions, oxygen acts as the significant oxidant by scavenging photo-induced electrons, and the single electron transfer from semiconductor to oxygen is often confirmed to be the key step, even the rate-determining step, of the overall reactions [29,30]. However, few works have been focused on the role of proton in the reactions in spite of the tremendous existence of protons in aqueous solution. In fact, the interfacial redox reactions of photocatalysts often include the simultaneous gain of electrons and protons [30–32]. The cleavage of protons or deuterium occurred in or influenced the rate-limiting step of the whole reaction in this term. Consequently, the roles and mechanisms of these proton coupled electron transfer processes are essential to be investigated because they can avoid the high-energy chemical intermediates caused by the local charge accumulation through moving the electron and proton together [30].

In this work, the  $\text{g-C}_3\text{N}_4$  was synthesized through a direct thermal decomposition of urea in air and bare  $\text{Bi}_{12}\text{GeO}_{20}$  was synthesized through a sol-gel method. To overcome the drawbacks of the pure  $\text{Bi}_{12}\text{GeO}_{20}$ , novel Z-scheme visible-light-driven  $\text{Bi}_{12}\text{GeO}_{20}/\text{g-C}_3\text{N}_4$  composites were synthesized by a one-step monolayer-dispersed method. The photocatalytic activities of  $\text{Bi}_{12}\text{GeO}_{20}/\text{g-C}_3\text{N}_4$  composites for the degradation of Rhodamine B (RhB) and microcystin-LR, and for reduction of aqueous Cr(VI) under visible-light irradiation were investigated. The oxygen-induced pathway of RhB and microcystin-LR degradation and proton assisted electron transfer mechanism of Cr(VI) reduction were discussed. Furthermore, a Z-scheme mechanism for the enhanced photocatalytic activities of the  $\text{Bi}_{12}\text{GeO}_{20}/\text{g-C}_3\text{N}_4$  composites was proposed.

## 2. Experimental

### 2.1. Synthesis of catalysts

All the reagents were of analytical purity and were used as received from Sinopharm Chemical Reagent Co., Ltd and J&K Chemical, Ltd. The  $\text{g-C}_3\text{N}_4$  was synthesized by direct heating urea in air.

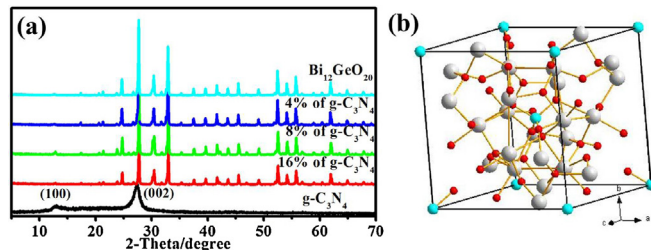


**Fig. 1.** (a) XRD patterns of bare  $\text{Bi}_{12}\text{GeO}_{20}$ ,  $\text{g-C}_3\text{N}_4$  and  $\text{Bi}_{12}\text{GeO}_{20}/\text{g-C}_3\text{N}_4$  composites with different contents of  $\text{g-C}_3\text{N}_4$ . (b) Supercell model of  $\text{Bi}_{12}\text{GeO}_{20}$ .

Typically, 10 g of urea powder was put into a ceramic crucible with a cover, and then heated to 550 °C in furnace for 2 h in air. The obtained yellow powder was collected without further treatment.

The bare  $\text{Bi}_{12}\text{GeO}_{20}$  particles were synthesized by a reported sol-gel method of our group [8]. For the further fabrication of the  $\text{Bi}_{12}\text{GeO}_{20}/\text{g-C}_3\text{N}_4$  composites, different amounts of  $\text{g-C}_3\text{N}_4$  (4%, 8% and 16% to the weight of  $\text{Bi}_{12}\text{GeO}_{20}$  respectively) were completely dispersed in ethanol assisted by 30 min of ultrasonication and then the as-prepared  $\text{Bi}_{12}\text{GeO}_{20}$  particles were added into the above solution and stirred for 24 h. The obtained products were collected by centrifugation, rinsed with distilled water and ethanol respectively, and then dried at 70 °C for 5 h.

### 2.2. Characterization

The structures of the  $\text{Bi}_{12}\text{GeO}_{20}/\text{g-C}_3\text{N}_4$  composites were determined by X-ray diffraction (XRD) analysis on a D/MAX-RB diffractometer with Cu K $\alpha$  radiation under the operation conditions of 40 kV and 50 mA. X-ray photoelectron spectroscopy (XPS) analysis for the  $\text{Bi}_{12}\text{GeO}_{20}/\text{g-C}_3\text{N}_4$  composites was performed by using a Thermo VG Multilab 2000 spectrometer (UK) with a monochromatic Al K $\alpha$  source. All binding energies were referred to the C 1s peak at 284.63 eV of the surface adventitious carbon and revised. The morphologies of the bare  $\text{Bi}_{12}\text{GeO}_{20}$  particles were characterized by the scanning electron microscopy (SEM, JSM-5610LV). The morphologies, microstructures and elemental distribution maps of the prepared  $\text{Bi}_{12}\text{GeO}_{20}/\text{g-C}_3\text{N}_4$  composites were further examined by transmission electron microscopy (TEM) and high-resolution transmission electron microscopy (HRTEM) using a JEM 2100F electron microscope operated at an accelerating voltage of 200 kV. A Nexus Fourier transform infrared (FT-IR) spectroscopy (Thermo Nicolet, USA) was used to detect the chemical bonds of the as-prepared  $\text{Bi}_{12}\text{GeO}_{20}/\text{g-C}_3\text{N}_4$  composites. The absorption edges of samples were detected by a UV-vis spectrophotometer (UV2550, Shimadzu Corporation, Kyoto, Japan).  $\text{BaSO}_4$  was used as a reflectance standard. The measurements of surface photovoltage spectroscopy (SPS) were carried out according to previous report [33]. Electron spin resonance (ESR) experiments were conducted with a Bruker EPR ELEXSYS 500 spectrometer (Bruker Co. Germany). The same quartz tube was used for all the measurements to minimize errors. Photoluminescence (PL) characteristics were examined on a fluorescence spectrophotometer (RF-5301 PC, Shimadzu, Japan).

### 2.3. Photocatalytic activity

The photocatalytic activities of the as-prepared  $\text{Bi}_{12}\text{GeO}_{20}/\text{g-C}_3\text{N}_4$  composites were measured by the degradation of RhB and microcystin-LR aqueous solution and reduction of aqueous Cr(VI) under visible-light irradiation. For the degradation of RhB aqueous solution, the experiments were performed at room temperature as follows: 0.3 g of the as-prepared catalyst was added into 100 mL of RhB aqueous solution (5 mg/L). Prior to visible-light illumina-

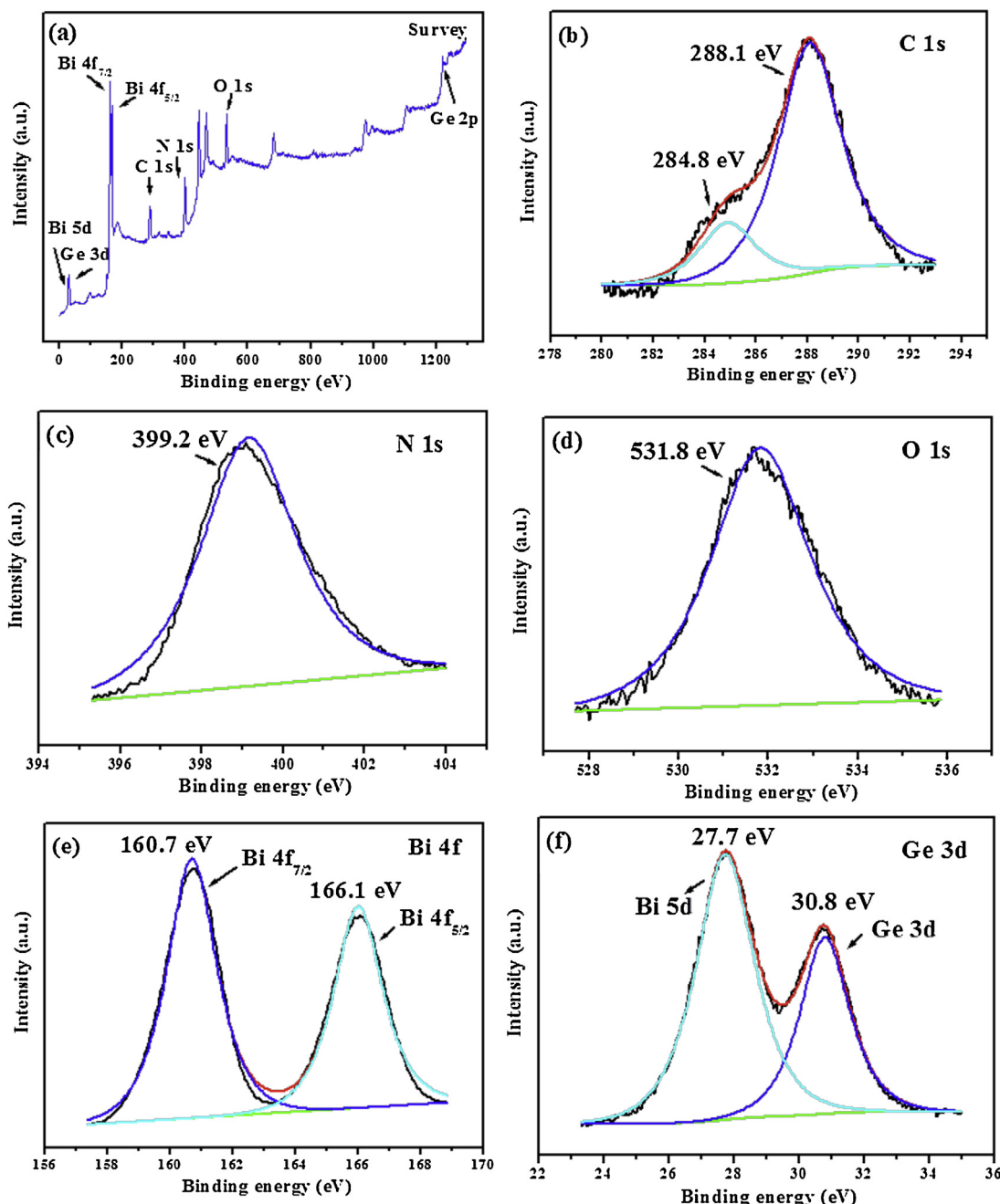


**Fig. 2.** XPS spectra of the  $\text{Bi}_{12}\text{GeO}_{20}/\text{g-C}_3\text{N}_4$  composites with 8% of  $\text{g-C}_3\text{N}_4$ : (a) survey spectrum, (b) C 1s spectrum, (c) N 1s spectrum, (d) O 1s spectrum, (e) Bi 4f spectrum, and (f) Ge 3d spectrum.

tion, the suspension was stirred for 30 min in dark to reach the adsorption-desorption equilibrium. The suspension was then irradiated with visible-light emitted by a 300 W Dy lamp with a 400 nm cutoff filter. The reaction temperature was kept at room temperature to prevent any thermal catalytic effect. At a defined time interval, the concentration of RhB aqueous solution was analyzed using a UV-vis spectrophotometer (UV751GD, China) at its maximum absorption wavelength of 553 nm.

For the degradation of microcystin-LR, the experiments were performed as follows: 0.02 g of the as-prepared samples was added in 20 mL of microcystin-LR solution with the initial concentration of 0.5 mg/L. Prior to visible-light illumination, the suspension was stirred for 30 min in dark to reach the adsorption-desorption equilibrium. The reaction temperature was kept at room temperature to prevent any thermal catalytic effect. At a defined time

interval, a certain volume of suspension was placed in vials and analyzed with high-performance liquid chromatography (HPLC, Agilent, 1260 infinity) for the quantification of microcystin-LR. For the HPLC analysis, the injection volume to a diamsil C-18 column was 20  $\mu\text{L}$ . The mobile phase in isocratic mode with a flow rate of 0.2 mL/min was a mixture of trifluoroacetic acid aqueous solution and methanol at a volume ratio of 13:7. The microcystin-LR was measured with a photodiode array detector at 238 nm.

For the reduction of aqueous Cr(VI), the experiments were performed at room temperature as follows: aqueous Cr(VI) solution was prepared by diluting the  $\text{K}_2\text{Cr}_2\text{O}_7$  standard solution with distilled water. 0.3 g of the as-prepared catalyst was added into 100 mL of aqueous Cr(VI) (10 mg/L, pH = 2.5). Prior to visible-light illumination, the suspension was stirred for 30 min in dark to reach the adsorption equilibrium. The suspension was then irradiated with

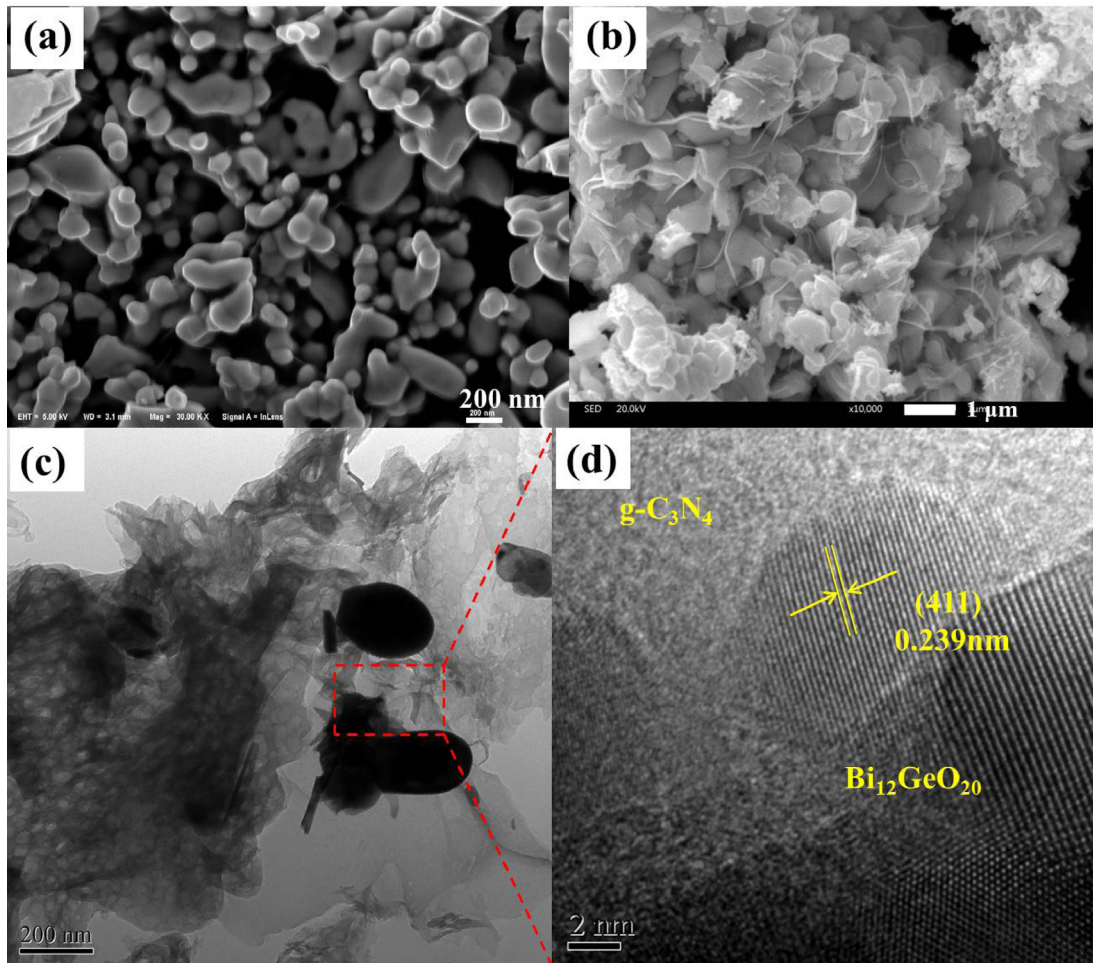


**Fig. 3.** (a) SEM image of  $\text{Bi}_{12}\text{GeO}_{20}$ . (b) SEM image of  $\text{Bi}_{12}\text{GeO}_{20}/\text{g-C}_3\text{N}_4$  composites with 8% of  $\text{g-C}_3\text{N}_4$ . (c) TEM and (d) HRTEM images of the  $\text{Bi}_{12}\text{GeO}_{20}/\text{g-C}_3\text{N}_4$  composites with 8% of  $\text{g-C}_3\text{N}_4$ .

visible-light emitted by a 300 W D<sub>y</sub> lamp with a 400 nm cutoff filter. The reaction temperature was kept at room temperature to prevent any thermal catalytic effect. During the photocatalytic reaction, 3.0 mL of the suspension was sampled at given time intervals and centrifuged to remove the photocatalyst. The Cr(VI) contents in the supernatant solutions were determined colorimetrically at 540 nm using the standard diphenylcarbazide method with a detection limit of 5  $\mu\text{g/L}$ . Kinetic isotope effect (KIE) values were defined as the ratio of the rate of conversion for Cr(VI) in  $\text{H}_2\text{O}$  and  $\text{D}_2\text{O}$ , respectively.

#### 2.4. Radical species trapping and ESR experiments

In radical species trapping experiments, 1,4-benzoquinone (BQ, 2 mM), isopropanol (IPA, 2 mM), and  $\text{Na}_2\text{C}_2\text{O}_4$  (2 mM) were used as the scavengers of  $\text{O}_2^{\bullet-}$ ,  $\text{h}^+$  and  $\cdot\text{OH}$  to investigate the active species in photocatalytic reaction, respectively. In ESR experiments, the  $\text{O}_2^{\bullet-}$  and  $\cdot\text{OH}$  species were trapped by the DMPO [14]. 10 mg of the as-prepared samples were dissolved in 0.5 mL of deionized water ( $\cdot\text{OH}$ ) or 0.5 mL of methanol ( $\text{O}_2^{\bullet-}$ ), and then 45  $\mu\text{L}$  of DMPO was added followed by ultrasonic dispersion for 5 min, respectively.

#### 2.5. In situ ATR-FTIR spectroscopy measurements

The in situ ATR-FTIR measurements were carried out on a Nicolet 6700 FT-IR with a MCT detector. Both sample and background spectra ranging from 4000 to 500  $\text{cm}^{-1}$  were recorded with a

resolution of 4  $\text{cm}^{-1}$ . Data were collected and analyzed by the OMNIC software. For the photocatalytic reaction, 20 g/L of suspension containing  $\text{Bi}_{12}\text{GeO}_{20}/\text{g-C}_3\text{N}_4$  composites with 8% of  $\text{g-C}_3\text{N}_4$  was dropped on a ZnSe crystal and dried to form a film. A layer of Cr(VI) solution was then dripped onto the surface of the ZnSe crystal with the film. The crystal was placed in dark for 1 h to reach the adsorption equilibrium before drying in the room temperature. Then the samples were exposed to the irradiation of xenon lamp with point source ( $\lambda \geq 400$ ) after flowing Ar for 30 min.

## 3. Results and discussion

### 3.1. Structure and morphology

The crystal structure and phase composition of the as-prepared samples were examined by XRD analysis. The XRD patterns of bare  $\text{Bi}_{12}\text{GeO}_{20}$  particles,  $\text{g-C}_3\text{N}_4$  and  $\text{Bi}_{12}\text{GeO}_{20}/\text{g-C}_3\text{N}_4$  composites were shown in Fig. 1a. In the pattern of  $\text{g-C}_3\text{N}_4$ , the strong peak at  $2\theta = 27.7^\circ$  is indexed to the (002) plane of  $\text{g-C}_3\text{N}_4$  (JCPDS Card no. 87-1526), which represents the stacking of conjugated aromatic system [34]. The small peak at  $2\theta = 13.0^\circ$  is indexed to the (100) plane of  $\text{g-C}_3\text{N}_4$ , which can be associated with the interlayer stacking of  $\text{g-C}_3\text{N}_4$  [35]. As seen from the patterns of  $\text{Bi}_{12}\text{GeO}_{20}/\text{g-C}_3\text{N}_4$  composites, all  $\text{Bi}_{12}\text{GeO}_{20}$  characteristic peaks of the composites with different amounts of  $\text{g-C}_3\text{N}_4$  are in good agreement with the XRD pattern of cubic structure  $\text{Bi}_{12}\text{GeO}_{20}$  (JCPDS Card no. 77-0861). This indicates that the coupled  $\text{g-C}_3\text{N}_4$  does not influence the lat-

tice structure of  $\text{Bi}_{12}\text{GeO}_{20}$ . Note that the (310) plane of  $\text{Bi}_{12}\text{GeO}_{20}$  is overlapped with the (002) plane of  $\text{g-C}_3\text{N}_4$ . The characteristic peaks of the  $\text{g-C}_3\text{N}_4$  were no found in the XRD patterns of  $\text{Bi}_{12}\text{GeO}_{20}/\text{g-C}_3\text{N}_4$  composites.

To investigate the surface compositions and chemical state of  $\text{Bi}_{12}\text{GeO}_{20}/\text{g-C}_3\text{N}_4$  composites, XPS analyses of the composite with 8% of  $\text{g-C}_3\text{N}_4$  were carried out (shown in Fig. 2). From Fig. 2a, the survey XPS spectrum indicates that composition of the  $\text{Bi}_{12}\text{GeO}_{20}/\text{g-C}_3\text{N}_4$  composites included C, N, O, Bi and Ge. As seen from Fig. 2b, the C 1s region can be divided into two different peaks at 284.8 and 288.1 eV. The peak at 284.8 eV can be ascribed to the adsorbed carbon on the composites, while the peak at 288.1 eV can be ascribed to the binding energy of  $\text{C}-(\text{N})_3$  group [36,37]. Fig. 2c shows that the peak at 399.2 eV can be assigned to N 1s, which can be attributed to  $\text{C}=\text{N}-\text{C}$  group according to previous reports [37,38]. As shown in Fig. 2d, the O 1s peak around 531.8 eV can be attributed to bridging oxygen atoms from  $\text{Bi}-\text{O}-\text{Bi}$  bonds [39]. Fig. 2e indicates that the Bi 4f region can be divided into two different peaks at 160.7 and 166.1 eV, which can be ascribed to the  $\text{Bi } 4f_{7/2}$  and  $\text{Bi } 4f_{5/2}$  levels, respectively [40]. As seen from Fig. 2f, the peak at 27.7 eV is assigned to Bi 5d and the peak at 30.8 eV is assigned to Ge 3d, indicating germanium in the sample exists in the form of  $\text{Ge}^{4+}$  [8,41].

The morphology, size and phase composition of the as-prepared samples were investigated by SEM, TEM and HRTEM analyses. Fig. 3a and b are the SEM images of the bare  $\text{Bi}_{12}\text{GeO}_{20}$  particles and  $\text{Bi}_{12}\text{GeO}_{20}/\text{g-C}_3\text{N}_4$  composites with 8% of  $\text{g-C}_3\text{N}_4$ . Fig. 3a shows that the obtained samples are distributed with a diameter arranged from 50 to 200 nm. Fig. 3b shows that the bare  $\text{Bi}_{12}\text{GeO}_{20}$  particles are bonded with  $\text{g-C}_3\text{N}_4$  nanoflakes together. Fig. 3c and d are the TEM and HRTEM images of the  $\text{Bi}_{12}\text{GeO}_{20}/\text{g-C}_3\text{N}_4$  composites (8% of  $\text{g-C}_3\text{N}_4$ ) respectively. In Fig. 3c, it can be observed that the  $\text{g-C}_3\text{N}_4$  has a typical transparent and flake-like morphology and the  $\text{Bi}_{12}\text{GeO}_{20}$  particles are adsorbed by the thin films of  $\text{g-C}_3\text{N}_4$ . From Fig. 3d, the lattice spacing of 0.239 nm is consistent with the (411) crystal plane of  $\text{Bi}_{12}\text{GeO}_{20}$  crystal (JCPDS no. 77-0861). Fig. S1a–f are the elemental mapping images of  $\text{Bi}_{12}\text{GeO}_{20}/\text{g-C}_3\text{N}_4$  composites (8% of  $\text{g-C}_3\text{N}_4$ ). Fig. S1a shows that  $\text{Bi}_{12}\text{GeO}_{20}$  particles are bonded on the thin films of  $\text{g-C}_3\text{N}_4$ . Fig. S1b–d indicate that Bi, Ge and O are distributed on the  $\text{Bi}_{12}\text{GeO}_{20}$  particles in the same region of Fig. S1a. Fig. S1e and f show that C and N are homogeneously distributed on the obtained composites. Additionally, the extra Ge, O, C and N can be attributed to the weak signals in Fig. S1c–f. These above results indicate the existence of intimate connection between the  $\text{Bi}_{12}\text{GeO}_{20}$  and  $\text{g-C}_3\text{N}_4$  in the composites.

The surface bond structures of the as-prepared samples were studied by FTIR spectroscopy. Fig. 4 shows the FT-IR spectra of bare  $\text{Bi}_{12}\text{GeO}_{20}$  particles,  $\text{g-C}_3\text{N}_4$  and a series of  $\text{Bi}_{12}\text{GeO}_{20}/\text{g-C}_3\text{N}_4$  composites with different contents of  $\text{g-C}_3\text{N}_4$ . In the FT-IR spectrum of bare  $\text{Bi}_{12}\text{GeO}_{20}$  particles, the bands in the 400–750 cm<sup>-1</sup> region can be ascribed to the stretching mode of Bi-O and Ge-O units. In the FT-IR spectrum of  $\text{g-C}_3\text{N}_4$ , the peak at 811 cm<sup>-1</sup> can be attributed to the out-of plane bending modes C–N heterocycles [38]. The peaks at 1247 cm<sup>-1</sup>, 1324 cm<sup>-1</sup>, 1414 cm<sup>-1</sup> and 1572 cm<sup>-1</sup> can be associated with the aromatic C–N stretching [42]. Meanwhile, the peak at 1632 cm<sup>-1</sup> can be ascribed to the C=N stretching vibration modes [42]. It can be seen that main characteristic peaks of  $\text{Bi}_{12}\text{GeO}_{20}$  and  $\text{g-C}_3\text{N}_4$  can be observed in all the spectra of the  $\text{Bi}_{12}\text{GeO}_{20}/\text{g-C}_3\text{N}_4$  composites and the intensities of the peaks of  $\text{g-C}_3\text{N}_4$  increased with increasing its content. Moreover, to further study the heterostructure of  $\text{Bi}_{12}\text{GeO}_{20}/\text{g-C}_3\text{N}_4$  composites, we have synthesized another two kinds of  $\text{Bi}_{12}\text{GeO}_{20}/\text{g-C}_3\text{N}_4$  composites (8% of  $\text{g-C}_3\text{N}_4$ ), in which the  $\text{g-C}_3\text{N}_4$  was calcinated from thiourea and melamine respectively through the same method. The physical mixture of  $\text{Bi}_{12}\text{GeO}_{20}/\text{g-C}_3\text{N}_4$  (8% of  $\text{g-C}_3\text{N}_4$ ) was also prepared. We have studied the FT-IR spectra of these four samples and

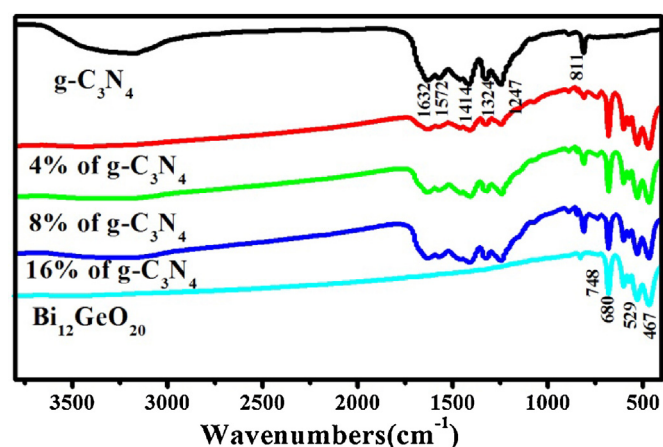


**Fig. 4.** FT-IR spectra of the bare  $\text{Bi}_{12}\text{GeO}_{20}$  particles,  $\text{g-C}_3\text{N}_4$  and a series of  $\text{Bi}_{12}\text{GeO}_{20}/\text{g-C}_3\text{N}_4$  composites with different contents of  $\text{g-C}_3\text{N}_4$ .

bare  $\text{Bi}_{12}\text{GeO}_{20}$  particles in Fig. S2. As shown in Fig. S2, all three kinds of  $\text{Bi}_{12}\text{GeO}_{20}/\text{g-C}_3\text{N}_4$  composites have an intensive absorption peak at 748 cm<sup>-1</sup> compared with that of the bare  $\text{Bi}_{12}\text{GeO}_{20}$  particles and physical mixture of  $\text{Bi}_{12}\text{GeO}_{20}/\text{g-C}_3\text{N}_4$ , implying that there is an interaction between  $\text{Bi}_{12}\text{GeO}_{20}$  and  $\text{g-C}_3\text{N}_4$  rather than a simply physical adsorption.

### 3.2. UV-vis DRS analysis

The optical properties of the as-prepared samples were investigated by UV-vis diffuse reflectance spectroscopy (UV-vis DRS). As shown in Fig. 5a, the absorption band edges of bare  $\text{Bi}_{12}\text{GeO}_{20}$  particles and pure  $\text{g-C}_3\text{N}_4$  are approximately located at 410 and 440 nm respectively. The absorption band edges of the  $\text{Bi}_{12}\text{GeO}_{20}/\text{g-C}_3\text{N}_4$  composites occurred obvious red shift as compared to that of the bare  $\text{Bi}_{12}\text{GeO}_{20}$  particles and the shift gradually increased when the content of  $\text{g-C}_3\text{N}_4$  increased from 4% to 16%, which indicates that the  $\text{Bi}_{12}\text{GeO}_{20}/\text{g-C}_3\text{N}_4$  composites have more favorable photo-absorption properties to cope with hazardous pollutants under visible-light irradiation. Furthermore, the optical band gap energy ( $E_g$ ) of semiconductor materials can be calculated by the following formula [10,43,44]:

$$\alpha h\nu = A(h\nu - E_g)^n/2$$

Where  $\alpha$ ,  $h\nu$ ,  $A$  and  $E_g$  represent the absorption coefficient, Planck constant, light frequency, proportionality and band gap energy, respectively.  $n$  is equal to 1 or 4, depending on whether the transition is direct or indirect, respectively. According to the previous reports [10,13], the fundamental absorption of  $\text{Bi}_{12}\text{GeO}_{20}$  involves a direct transition, while that of the  $\text{g-C}_3\text{N}_4$  has an indirect transition between bands. Thus, the band gap energy of the  $\text{g-C}_3\text{N}_4$  was calculated via a plot of the  $(Ah\nu)^{1/2}$  versus  $h\nu$ , and that of the  $\text{Bi}_{12}\text{GeO}_{20}$  was determined from a plot of the  $(Ah\nu)^2$  versus  $h\nu$ . As shown in Fig. 5b, the band gaps of the  $\text{g-C}_3\text{N}_4$  and  $\text{Bi}_{12}\text{GeO}_{20}$  were estimated to be 2.62 eV and 3.03 eV respectively.

### 3.3. Photocatalytic activity

RhB, microcystin-LR and Cr(VI) aqueous solutions were chosen as the model organic pollutants to evaluate the photocatalytic activities of the as-prepared catalysts. Fig. 6a displays the degradation ratio of RhB under different conditions, where  $C$  was the concentration of RhB after irradiation and  $C_0$  was the concentration of RhB after adsorption for 30 min in the dark. From Fig. 6a, the blank experiment indicates that the photolysis of the RhB

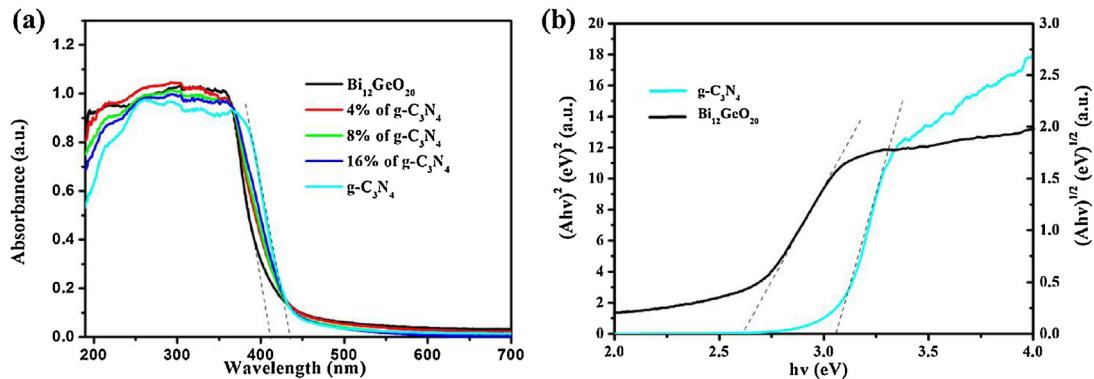


**Fig. 5.** (a) UV-vis diffuse reflection spectra of bare  $\text{Bi}_{12}\text{GeO}_{20}$  particles,  $\text{g-C}_3\text{N}_4$  and a series of  $\text{Bi}_{12}\text{GeO}_{20}/\text{g-C}_3\text{N}_4$  composites. (b) Plot of the  $(\text{Ahv})^2$  versus  $\text{hv}$  for bare  $\text{Bi}_{12}\text{GeO}_{20}$  particles and the  $(\text{Ahv})^{1/2}$  versus  $\text{hv}$  for  $\text{g-C}_3\text{N}_4$ .

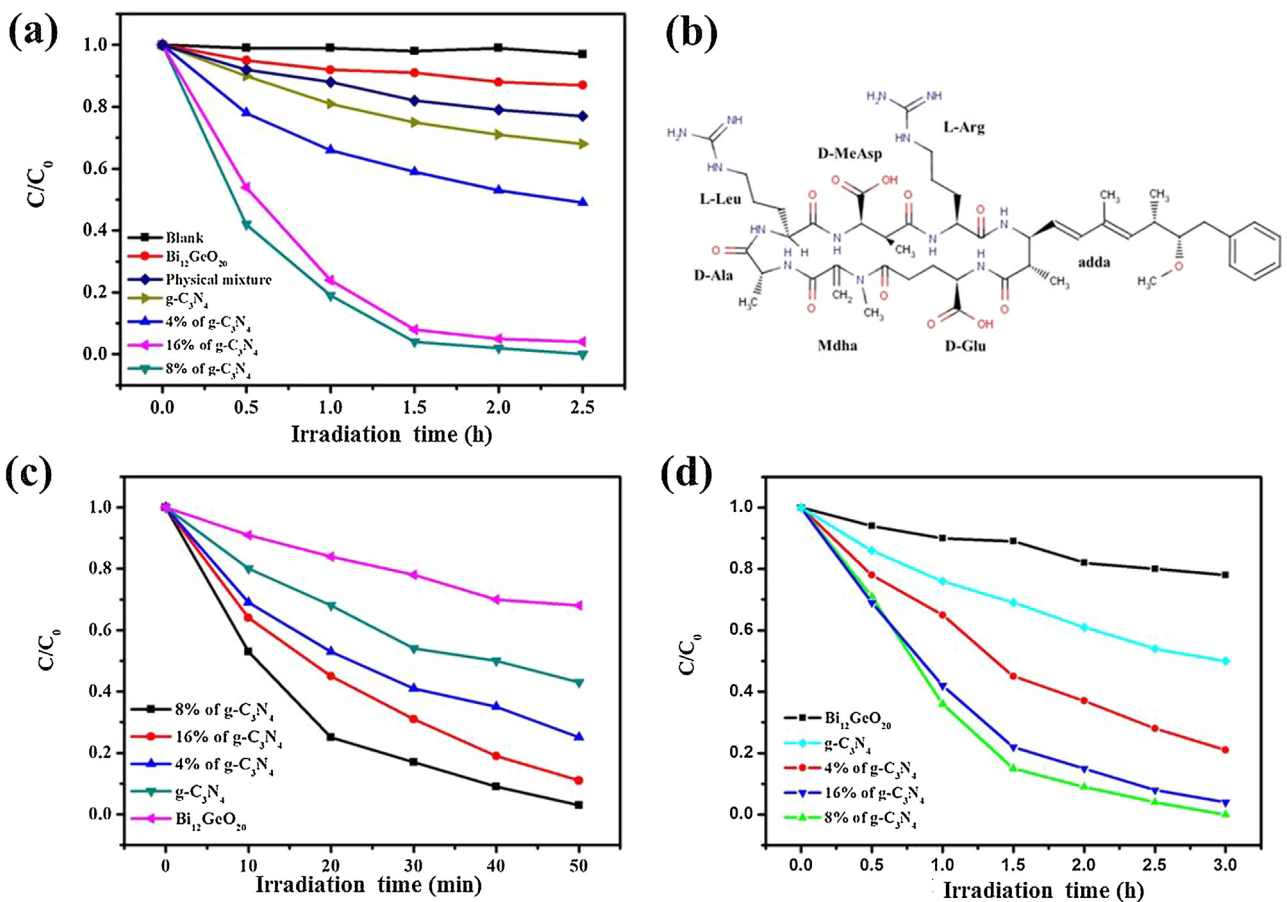


**Fig. 6.** (a) Photocatalytic degradation of RhB solution over the as-prepared samples. (b) The structure of microcystin-LR. (c) Photocatalytic degradation of microcystin-LR solution over the as-prepared different samples. (d) Photocatalytic reduction curves of aqueous Cr(VI) over the bare  $\text{Bi}_{12}\text{GeO}_{20}$  particles,  $\text{g-C}_3\text{N}_4$  and a series of  $\text{Bi}_{12}\text{GeO}_{20}/\text{g-C}_3\text{N}_4$  composites under visible-light irradiation.

aqueous solution was negligible in the absence of photocatalyst, implying that the RhB aqueous solution is stable under visible-light irradiation. Meanwhile, the pure  $\text{g-C}_3\text{N}_4$  and bare  $\text{Bi}_{12}\text{GeO}_{20}$  particles displayed low photocatalytic activities under visible-light irradiation. However, it can be seen that the as-prepared  $\text{Bi}_{12}\text{GeO}_{20}/\text{g-C}_3\text{N}_4$  composites enhanced the photocatalytic degradation ratio of RhB obviously. When the content of  $\text{g-C}_3\text{N}_4$  is 8%, the as-prepared composites exhibited the highest photocatalytic activity, and the photocatalyst can degrade RhB by 100% after 2.5 h. The  $\text{Bi}_{12}\text{GeO}_{20}/\text{g-C}_3\text{N}_4$  composites possessed superior photocatalytic capability than pure  $\text{Bi}_{12}\text{GeO}_{20}$  or  $\text{g-C}_3\text{N}_4$ , which can be ascribed to

the interaction of heterogeneous structures. Although the adding of  $\text{g-C}_3\text{N}_4$  is favorable to the charge transfer, excess  $\text{g-C}_3\text{N}_4$  would offer as the recombination centers of electron-hole pairs, leading to a less photocatalytic activity [45]. Therefore, the photocatalytic activity of  $\text{Bi}_{12}\text{GeO}_{20}/\text{g-C}_3\text{N}_4$  composites decreased when the content of  $\text{g-C}_3\text{N}_4$  was increased to 16%.

Additionally, the photocatalytic activity of the physical mixture of 8%  $\text{g-C}_3\text{N}_4$  and  $\text{Bi}_{12}\text{GeO}_{20}$  was also studied. The physical mixture was prepared through physical grind. In Fig. 6a, The  $\text{Bi}_{12}\text{GeO}_{20}/\text{g-C}_3\text{N}_4$  composites (8% of  $\text{g-C}_3\text{N}_4$ ) showed higher photocatalytic activity than that of the physical mixture sample, indicating the

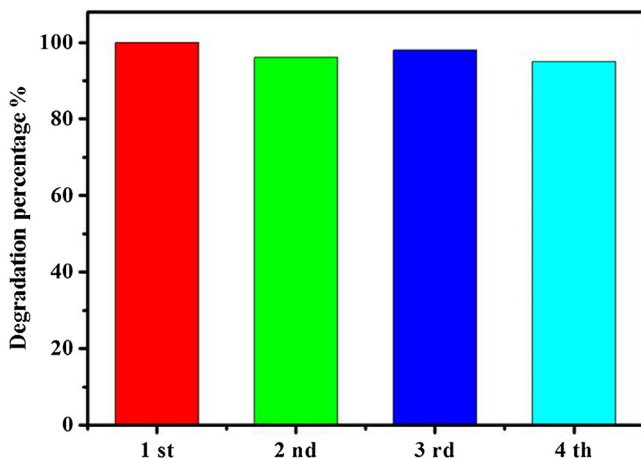


**Fig. 7.** Cycle runs of the  $\text{Bi}_{12}\text{GeO}_{20}/\text{g-C}_3\text{N}_4$  composites (8% of  $\text{g-C}_3\text{N}_4$ ) for degradation of RhB solution under visible-light irradiation.

formation of heterostructure in the composites enhanced the separation efficiency of the photo-induced carriers. Furthermore, the photocatalytic reactions were described by the first-order kinetics with respect to the concentration of RhB solution. Fig. S3 shows a comparison of the apparent rate constants ( $\text{h}^{-1}$ ) of the bare  $\text{Bi}_{12}\text{GeO}_{20}$ , pure  $\text{g-C}_3\text{N}_4$ , physical mixture sample and  $\text{Bi}_{12}\text{GeO}_{20}/\text{g-C}_3\text{N}_4$  composites with 4%, 8% and 16% of  $\text{g-C}_3\text{N}_4$  respectively. The results are 0.067, 0.184, 0.120, 0.347, 1.992 and 1.535 respectively.

Microcystin-LR (Fig. 6b) is a kind of toxic cyclic peptide released by cyanobacteria during algal blooms in eutrophic waters [46]. The photocatalytic oxidation activities of the  $\text{Bi}_{12}\text{GeO}_{20}/\text{g-C}_3\text{N}_4$  composites were further investigated by the degradation of microcystin-LR aqueous solution under visible-light irradiation. As shown in Fig. 6c, the as-prepared  $\text{Bi}_{12}\text{GeO}_{20}/\text{g-C}_3\text{N}_4$  composites showed enhanced photocatalytic activities obviously. Among them, the composites with 8% of  $\text{g-C}_3\text{N}_4$  displayed the highest degradation rate. Only in 50 min 97% of the microcystin-LR was degraded. These results are similar to the RhB degradation above.

The photocatalytic activities of the  $\text{Bi}_{12}\text{GeO}_{20}/\text{g-C}_3\text{N}_4$  composites for aqueous Cr(VI) reduction under visible-light irradiation were also tested. Fig. 6d shows the visible-light photocatalytic reduction of aqueous Cr(VI) over the bare  $\text{Bi}_{12}\text{GeO}_{20}$  particles,  $\text{g-C}_3\text{N}_4$  and  $\text{Bi}_{12}\text{GeO}_{20}/\text{g-C}_3\text{N}_4$  composites with different contents of  $\text{g-C}_3\text{N}_4$ . As we can see, all of the as-prepared samples could reduce the aqueous Cr(VI) under visible-light irradiation. The photocatalytic activities of the  $\text{Bi}_{12}\text{GeO}_{20}/\text{g-C}_3\text{N}_4$  composites were much higher than that of the pure  $\text{Bi}_{12}\text{GeO}_{20}$  or  $\text{g-C}_3\text{N}_4$ . After 3 h of visible-light irradiation, the reduction ratios of aqueous Cr(VI) over the  $\text{Bi}_{12}\text{GeO}_{20}$  particles and  $\text{g-C}_3\text{N}_4$  were 22% and 50% respectively. As for the  $\text{Bi}_{12}\text{GeO}_{20}/\text{g-C}_3\text{N}_4$  composites, the content of  $\text{g-C}_3\text{N}_4$  has a significant influence on the photocatalytic activities. When the  $\text{g-C}_3\text{N}_4$  content was changed from 4% to 8%, the photocatalytic reduction ratio was obviously improved and almost 100% of the aqueous Cr(VI) was reduced after 3 h of the visible-light irradiation. Meanwhile, when the content of  $\text{g-C}_3\text{N}_4$  was further increased from 8% to 16%, the photocatalytic activities of the  $\text{Bi}_{12}\text{GeO}_{20}/\text{g-C}_3\text{N}_4$  composites decreased, which is similar to the results of RhB degradation above.

To test the stability of the as-prepared  $\text{Bi}_{12}\text{GeO}_{20}/\text{g-C}_3\text{N}_4$  composites, the recycling capability of the composites with 8% of  $\text{g-C}_3\text{N}_4$  was evaluated by the degradation of the RhB aqueous solution in Fig. 7. From Fig. 7, it can be seen that the sample did not exhibit evident loss of photocatalytic activity after four recycles. Furthermore, we also studied the XRD and FT-IR patterns of the  $\text{Bi}_{12}\text{GeO}_{20}/\text{g-C}_3\text{N}_4$  composites (8% of  $\text{g-C}_3\text{N}_4$ ) after photocatalytic degradation in Figs.

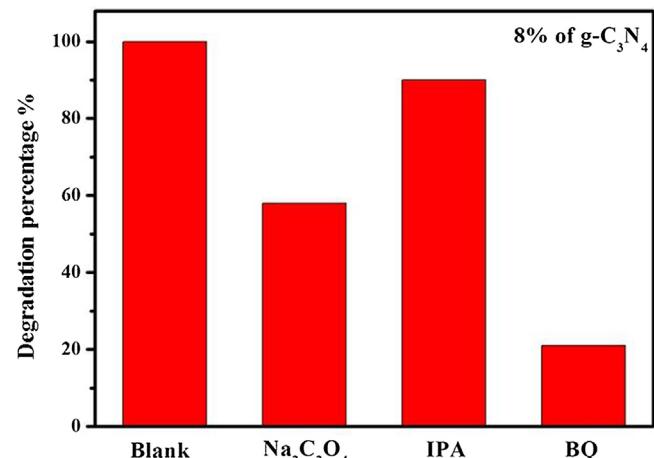


**Fig. 8.** Photocatalytic activities of the  $\text{Bi}_{12}\text{GeO}_{20}/\text{g-C}_3\text{N}_4$  composites with 8% of  $\text{g-C}_3\text{N}_4$  for the degradation of RhB solution in the presence of different scavengers under visible-light irradiation.

S4 and S5 respectively. The XRD and FT-IR patterns of the original and recovered samples did not exhibit evident changes, which indicate that the  $\text{Bi}_{12}\text{GeO}_{20}/\text{g-C}_3\text{N}_4$  composites are effective and stable catalysts for the degradation of contaminations.

### 3.4. Mechanism of the photocatalytic activity

Radical species ( $\cdot\text{OH}$ ,  $\text{O}_2^{\bullet-}$  and  $\text{h}^+$ ) trapping experiments and ESR analyses were carried out to investigate the reaction mechanism of the  $\text{Bi}_{12}\text{GeO}_{20}/\text{g-C}_3\text{N}_4$  composites for the degradation of RhB solution. In the radical species trapping experiments, BQ, IPA, and  $\text{Na}_2\text{C}_2\text{O}_4$  were used as the scavengers of  $\text{O}_2^{\bullet-}$ ,  $\text{h}^+$  and  $\cdot\text{OH}$  respectively to investigate the active species in photocatalytic reaction. Fig. 8 shows the degradation ratio of RhB solution over the  $\text{Bi}_{12}\text{GeO}_{20}/\text{g-C}_3\text{N}_4$  composites with 8% of  $\text{g-C}_3\text{N}_4$  in the presence of different scavengers. It can be seen that the BQ and  $\text{Na}_2\text{C}_2\text{O}_4$  had significant effects on the photocatalytic activity of the composites, which suggests that the  $\text{O}_2^{\bullet-}$  and  $\text{h}^+$  are the mainly active species in the photocatalytic oxidation process.

ESR analyses were used to further investigate the existence of  $\text{O}_2^{\bullet-}$  and  $\cdot\text{OH}$  species in the photocatalytic reaction systems of  $\text{g-C}_3\text{N}_4$ ,  $\text{Bi}_{12}\text{GeO}_{20}$  and  $\text{Bi}_{12}\text{GeO}_{20}/\text{g-C}_3\text{N}_4$  composites with 8% of  $\text{g-C}_3\text{N}_4$ . Fig. 9a shows the ESR signals of DMPO- $\cdot\text{OH}$  over the as-prepared samples. Four characteristic peaks of the DMPO- $\cdot\text{OH}$  adducts can be observed for all the samples, which indicates that the  $\cdot\text{OH}$  species were generated in the photocatalytic reaction [13]. It is worth to note that the curves for all the samples are not strong, which shows that the generated  $\cdot\text{OH}$  species are few in the reaction. From Fig. 9b, six characteristic peaks of the DMPO- $\text{O}_2^{\bullet-}$  adducts can be observed obviously for  $\text{g-C}_3\text{N}_4$  and  $\text{Bi}_{12}\text{GeO}_{20}/\text{g-C}_3\text{N}_4$  composites with 8% of  $\text{g-C}_3\text{N}_4$  respectively, indicating the  $\text{O}_2^{\bullet-}$  species were produced after irradiation for these two samples [14]. No obvious signal could be observed for the bare  $\text{Bi}_{12}\text{GeO}_{20}$ . Considering the rare content of  $\text{g-C}_3\text{N}_4$  in the composites, it can be concluded that the separation efficiency of photo-induced electron-hole pairs in  $\text{Bi}_{12}\text{GeO}_{20}/\text{g-C}_3\text{N}_4$  composites is higher than single  $\text{g-C}_3\text{N}_4$ . Furthermore, it can be seen clearly that the curves of DMPO- $\text{O}_2^{\bullet-}$  adducts are much higher than that of the DMPO- $\cdot\text{OH}$  adducts for the  $\text{Bi}_{12}\text{GeO}_{20}/\text{g-C}_3\text{N}_4$  composites with 8% of  $\text{g-C}_3\text{N}_4$ , which further indicates that the  $\text{O}_2^{\bullet-}$  are the main active species in the photocatalytic process. On the basis of the above results, it can be concluded that the transfer of electrons from the as-prepared composites to oxygen is significant to the reaction and the photocatalytic oxi-

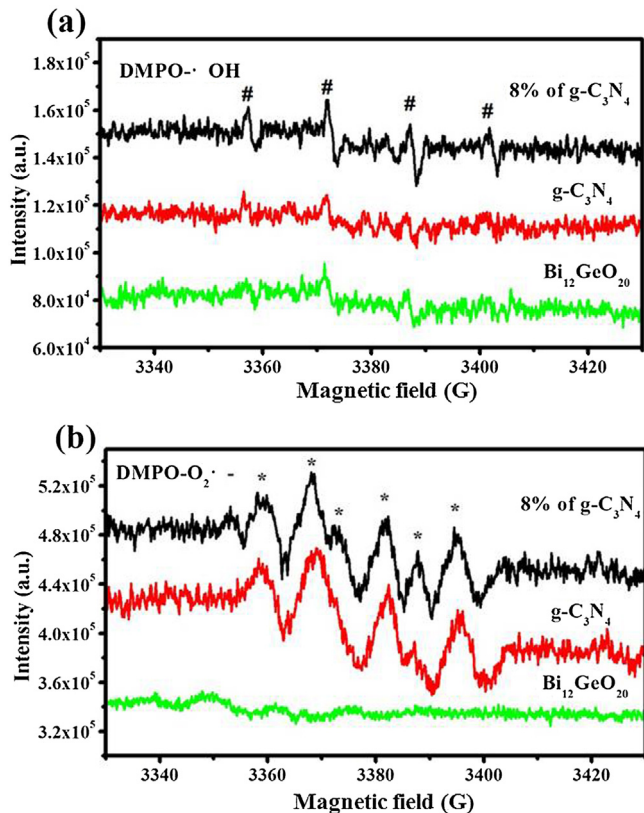


Fig. 9. ESR signals of the (a) DMPO-•O<sub>2</sub><sup>-</sup> and (b) DMPO-•OH for g-C<sub>3</sub>N<sub>4</sub>, Bi<sub>12</sub>GeO<sub>20</sub> and Bi<sub>12</sub>GeO<sub>20</sub>/g-C<sub>3</sub>N<sub>4</sub> composites with 8% of g-C<sub>3</sub>N<sub>4</sub> irradiated for 60 s.

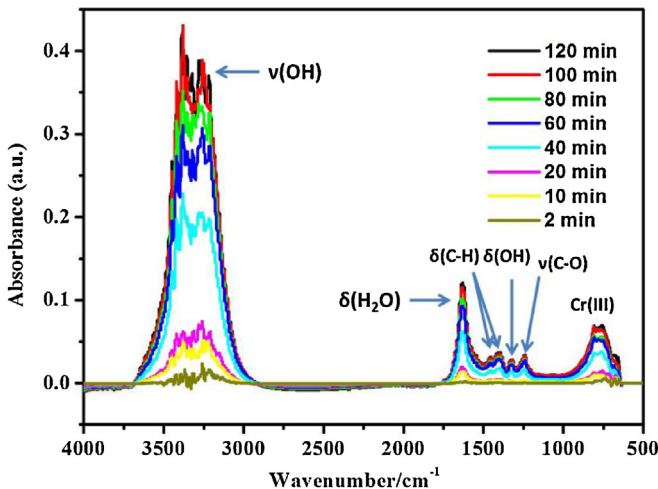


Fig. 10. Time series ATR-FTIR spectra for the photocatalytic reduction of aqueous Cr(VI) solution on Bi<sub>12</sub>GeO<sub>20</sub>/g-C<sub>3</sub>N<sub>4</sub> composites with 8% of g-C<sub>3</sub>N<sub>4</sub> irradiated from 2 to 120 min.

dation process of organic pollutants is a typically oxygen-induced radical reactions.

In situ ATR-FTIR analyses were performed to investigate the pathway for the photocatalytic reduction of Cr(VI) solution of the Bi<sub>12</sub>GeO<sub>20</sub>/g-C<sub>3</sub>N<sub>4</sub> composites. Fig. 10 indicates the time series ATR-FTIR spectra for the photocatalytic reduction of Cr(VI) solution on Bi<sub>12</sub>GeO<sub>20</sub>/g-C<sub>3</sub>N<sub>4</sub> composites with 8% of g-C<sub>3</sub>N<sub>4</sub> irradiated from 2 to 120 min. As shown in Fig. 10, three water species were observed. The huge broad absorption band ranging from 3700 to 3000 cm<sup>-1</sup> can be attributed to ν(OH) [32]. The peaks at about 1635 and 1310 cm<sup>-1</sup> can be assigned to the δ(H<sub>2</sub>O) and δ(OH) respec-

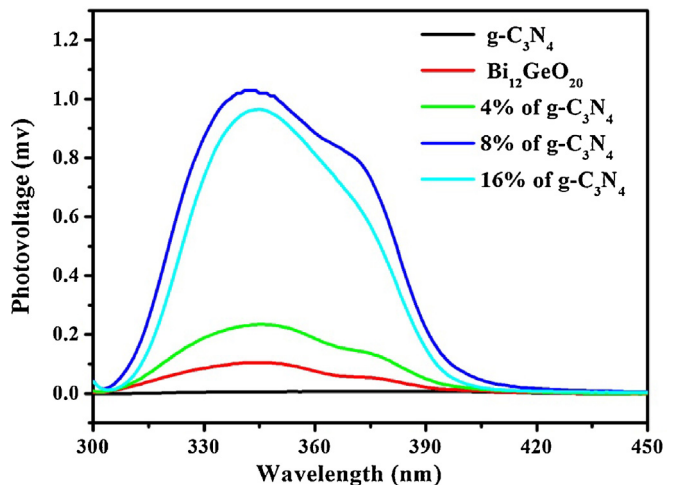
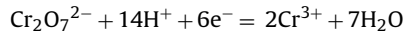
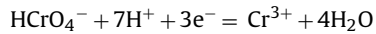


Fig. 11. Surface photovoltage spectroscopy of the as-prepared photocatalysts.

tively [32]. The absorption band located below 1000 cm<sup>-1</sup> may be attributed to Cr-O caused by the absorption of Cr(III) [47,48]. In addition, the δ(C-H) located at 1460 and 1405 cm<sup>-1</sup> respectively and ν(C=O) located at 1260 cm<sup>-1</sup> were also observed. It can be seen that all the peaks especially for three water species increased during the irradiation. This result confirms that the water was produced during the reaction. Furthermore, hydrogen/deuterium (H/D) kinetic isotope study revealed that the KIE values for Bi<sub>12</sub>GeO<sub>20</sub>/g-C<sub>3</sub>N<sub>4</sub> composites with different content of g-C<sub>3</sub>N<sub>4</sub> were 1.27, 1.21 and 1.13 respectively (from 4% to 16% of g-C<sub>3</sub>N<sub>4</sub>). This normal secondary KIE values indicate the non-negligible influence of proton transfer in the reduction of Cr(VI) even through the cleavage of H/D did not occur in the rate-limiting step and this reaction is a proton assisted electron transfer process. Meanwhile, previous reports have shown that the major Cr(VI) states in acidic aqueous solution (pH = 2–4) were HCrO<sub>4</sub><sup>-</sup> and Cr<sub>2</sub>O<sub>7</sub><sup>2-</sup> [47,49]. The proton assisted electron transfer pathway of Cr(VI) reduction can be described as the following formula [49,50]:



Surface photovoltage spectroscopy (SPS) were used to further investigate the enhancement of separation efficiency of the photo-induced electron-hole pairs. Generally speaking, the strong SPS response is in accord with the high separation efficiency of the photo-induced carriers on the basis of the SPS principle [51–53]. From Fig. 11, all the samples displayed SPS response peaks at around 350 nm. The Bi<sub>12</sub>GeO<sub>20</sub>/g-C<sub>3</sub>N<sub>4</sub> composites with 8% of g-C<sub>3</sub>N<sub>4</sub> exhibited the most intensive peak and the intensity of SPS responses over the as-prepared samples decreased in the order of 8% g-C<sub>3</sub>N<sub>4</sub> > 16% g-C<sub>3</sub>N<sub>4</sub> > 4% g-C<sub>3</sub>N<sub>4</sub> > Bi<sub>12</sub>GeO<sub>20</sub> > g-C<sub>3</sub>N<sub>4</sub>. These results indicate that the heterostructure of Bi<sub>12</sub>GeO<sub>20</sub>/g-C<sub>3</sub>N<sub>4</sub> composites is beneficial to improve the separation efficiency of the photo-induced carriers. The photoluminescence (PL) characteristic was also used to study the separation efficiency of the as-prepared samples [54,55]. To investigate the important role of the heterostructure of Bi<sub>12</sub>GeO<sub>20</sub>/g-C<sub>3</sub>N<sub>4</sub> composites, we have synthesized the composites of montmorillonite loaded with 8% of g-C<sub>3</sub>N<sub>4</sub> (MMT-g-C<sub>3</sub>N<sub>4</sub>) through the physical grind. As shown in Fig. S6, the PL intensity of Bi<sub>12</sub>GeO<sub>20</sub>/g-C<sub>3</sub>N<sub>4</sub> composites was significantly reduced as compared to that of the pure g-C<sub>3</sub>N<sub>4</sub> and MMT-g-C<sub>3</sub>N<sub>4</sub>, implying a lower recombination probability of free charges in the Bi<sub>12</sub>GeO<sub>20</sub>/g-C<sub>3</sub>N<sub>4</sub> composites.

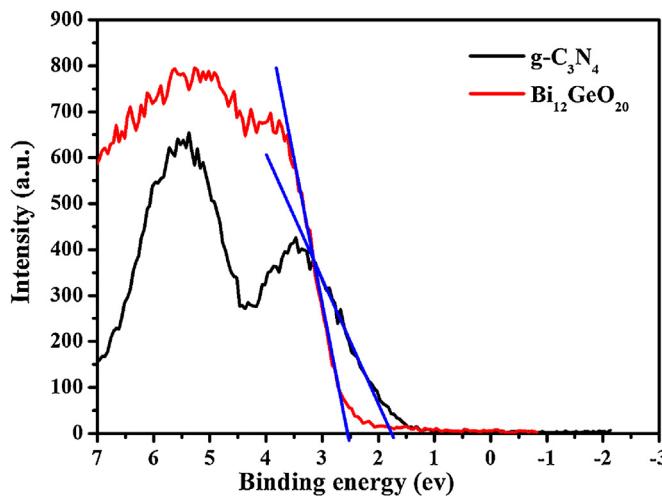


Fig. 12. VB-XPS spectra of  $\text{Bi}_{12}\text{GeO}_{20}$  and  $\text{g-C}_3\text{N}_4$ .

To further investigate the reasons of the enhanced separation efficiency of the photo-induced electron-hole pairs. The band edge positions of  $\text{Bi}_{12}\text{GeO}_{20}$  and  $\text{g-C}_3\text{N}_4$  were determined by the VB-XPS in Fig. 12. As shown in Fig. 12, the energy differences between the Fermi levels and the valence bands of the as-prepared  $\text{Bi}_{12}\text{GeO}_{20}$  and  $\text{g-C}_3\text{N}_4$  are 2.55 and 1.80 eV respectively. According to the earlier reports, the Fermi levels of the  $\text{Bi}_{12}\text{GeO}_{20}$  and  $\text{g-C}_3\text{N}_4$  are 0.23 and  $-0.30$  eV respectively [56,57]. Considering the band gaps of the  $\text{Bi}_{12}\text{GeO}_{20}$  and  $\text{g-C}_3\text{N}_4$ , the valance band ( $E_{VB}$ ) and conduction band ( $E_{CB}$ ) of  $\text{Bi}_{12}\text{GeO}_{20}$  and  $\text{g-C}_3\text{N}_4$  were calculated to be  $2.78/-0.25$  eV and  $1.50/-1.12$  eV respectively.

According to the above calculated results, the schematic illustration of band structure diagram of  $\text{Bi}_{12}\text{GeO}_{20}/\text{g-C}_3\text{N}_4$  composites was shown in Fig. 13. The transfer path of the photo-induced carriers can be described in Fig. 13a and b respectively. If the carriers of  $\text{Bi}_{12}\text{GeO}_{20}/\text{g-C}_3\text{N}_4$  composites transferred according to the path in Fig. 13a, the electrons in the  $E_{CB}$  of  $\text{g-C}_3\text{N}_4$  will migrate to the  $E_{CB}$  of  $\text{Bi}_{12}\text{GeO}_{20}$ , and the holes in the  $E_{VB}$  of  $\text{Bi}_{12}\text{GeO}_{20}$  will migrate to the  $E_{VB}$  of  $\text{g-C}_3\text{N}_4$ . As a result, the electrons accumulated in the  $E_{CB}$  of  $\text{Bi}_{12}\text{GeO}_{20}$  could not reduce  $\text{O}_2$  to yield  $\text{O}_2^{\bullet-}$  ( $\text{O}_2/\text{O}_2^{\bullet-} = -0.33$  eV vs. NHE), which is against to the results of radical species trapping

and ESR experiments above. Consequently, the proposed reaction mechanism in  $\text{Bi}_{12}\text{GeO}_{20}/\text{g-C}_3\text{N}_4$  composites for the degradations of microcystin-LR and RhB aqueous solution and reduction of aqueous Cr(VI) can be described in Fig. 13b. From Fig. 13b, the transfer and separation of the photo-induced electron-hole pairs followed a direct Z-scheme path, in which the fast combination was achieved between the electrons in the  $E_{CB}$  of  $\text{Bi}_{12}\text{GeO}_{20}$  and the holes in the  $E_{VB}$  of  $\text{g-C}_3\text{N}_4$ . As shown in Fig. 13c, the photo-induced electrons of  $\text{g-C}_3\text{N}_4$  were accumulated to yield  $\text{O}_2^{\bullet-}$  or reacted with Cr(VI) according to the proton assisted electron transfer process, while holes of the  $\text{Bi}_{12}\text{GeO}_{20}$  would react with organic substrates directly.

Based on the above results, it can be seen that the degradation of microcystin-LR and RhB solution followed an oxygen-induced radical pathway while the reduction of aqueous Cr(VI) were carried out through a proton assisted electron transfer process. The heterostructure of  $\text{Bi}_{12}\text{GeO}_{20}/\text{g-C}_3\text{N}_4$  composites has a significant effect on the separation efficiency of the photo-induced carriers. The transfer and separation of photo-induced electron-hole pairs of the as-prepared  $\text{Bi}_{12}\text{GeO}_{20}/\text{g-C}_3\text{N}_4$  composites followed a direct Z-scheme path which is favorable to improve the photocatalytic activities under visible-light irradiation.

#### 4. Conclusion

In summary, the novel  $\text{Bi}_{12}\text{GeO}_{20}/\text{g-C}_3\text{N}_4$  composites were successfully synthesized via a one-step monolayer-dispersed method. The UV-vis DRS results proved that the  $\text{Bi}_{12}\text{GeO}_{20}/\text{g-C}_3\text{N}_4$  composites have more favorable photo-absorption properties as compared to the pure  $\text{Bi}_{12}\text{GeO}_{20}$ . The radical species trapping and ESR experiments showed that the microcystin-LR and RhB degradation followed an oxygen-induced pathway. The in situ ATR-FTIR spectroscopy measurements and kinetic isotope study indicated that the photocatalytic reduction of aqueous Cr(VI) is a proton assisted electron transfer reaction. The SPS analysis indicated that the  $\text{Bi}_{12}\text{GeO}_{20}/\text{g-C}_3\text{N}_4$  composites exhibited more effective separation efficiency of photo-induced electron-hole pairs as compared to pure  $\text{Bi}_{12}\text{GeO}_{20}$  or  $\text{g-C}_3\text{N}_4$ . The as-prepared  $\text{Bi}_{12}\text{GeO}_{20}/\text{g-C}_3\text{N}_4$  composites exhibited enhanced photocatalytic activities for the degradation of microcystin-LR and RhB aqueous solution and reduction of aqueous Cr(VI) under visible-light irradiation due to the improved photo-absorption properties and more

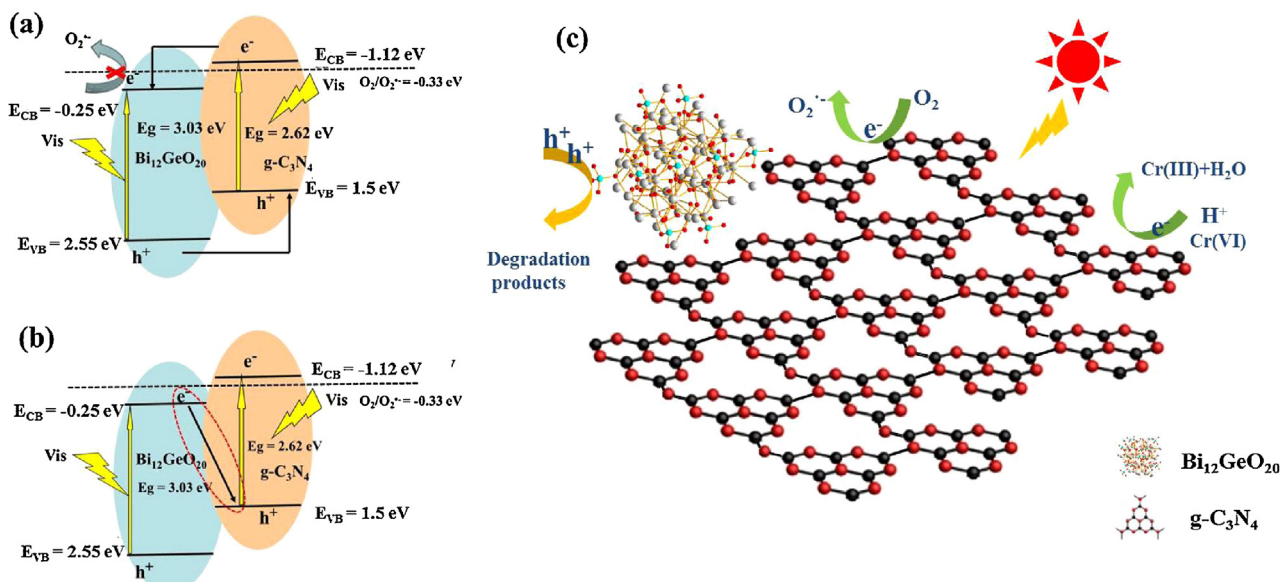


Fig. 13. Schematic illustration of band structure diagram and photo-induced carriers transfer of  $\text{Bi}_{12}\text{GeO}_{20}/\text{g-C}_3\text{N}_4$  composites under visible-light irradiation.

effective transfer of the photo-induced carriers caused by the Z-scheme photocatalytic reaction path. This study demonstrates that  $\text{Bi}_{12}\text{GeO}_{20}/\text{g-C}_3\text{N}_4$  photocatalyst is a very promising candidate for developing visible-light-responsive materials with high photocatalytic activities.

## Acknowledgments

This work was supported by the National Natural Science Foundation of China (NSFC No.51472194) and the National Basic Research Program of China (973 Program No.2013CB632402). This research was also partly supported by JSPS KAKENHI Grant Number JP16H06439 (Grant-in-Aid for Scientific Research on Innovative Areas), the Dynamic Alliance for Open Innovation Bridging Human, Environment and Materials, the Cooperative Research Program of "Network Joint Research Center for Materials and Devices".

## Appendix A. Supplementary data

Supplementary data associated with this article can be found, in the online version, at <http://dx.doi.org/10.1016/j.apcatb.2017.02.014>.

## References

- [1] G. Wang, B.B. Huang, Z.J. Li, Z.Z. Lou, Z.Y. Wang, Y. Dai, M.H. Whango, *Sci. Rep.* 5 (2015) 8544.
- [2] X.Y. Li, H.M. Yang, *Appl. Clay Sci.* 100 (2014) 43–49.
- [3] L. Zhang, X.L. Fu, S.G. Meng, X.L. Jiang, J.H. Wang, S.F. Chen, *J. Mater. Chem. A* 3 (2015) 23732–23742.
- [4] Y.L. Zheng, W.Z. Wang, D. Jiang, L. Zhang, X.M. Li, Z. Wang, *J. Mater. Chem. A* 4 (2016) 105–112.
- [5] Y.Y. Zhu, Y.F. Liu, Y.H. Lv, Q. Ling, D. Liu, Y.F. Zhu, *J. Mater. Chem. A* 2 (2014) 13041–13048.
- [6] H.H. Gan, G.K. Zhang, H.X. Huang, *J. Hazard. Mater.* 250 (2013) 131–137.
- [7] L. Zhang, W.Z. Wang, S.M. Sun, D. Jiang, E. Gao, *Appl. Catal. B: Environ.* 162 (2015) 470–474.
- [8] Z. Wan, G.K. Zhang, *Sci. Rep.* 4 (2014) 6298.
- [9] C.H. He, M.Y. Gu, *Scr. Mater.* 54 (2006) 1221–1225.
- [10] D.F. Hou, X.L. Hu, Y.W. Wen, B. Shan, P. Hu, X.Q. Xiong, Y. Qiao, Y.H. Huang, *Phys. Chem. Chem. Phys.* 15 (2013) 20698–20705.
- [11] Z.H. Chen, W.L. Wang, Z.G. Zhang, X.M. Fang, *J. Phys. Chem. C* 117 (2013) 19346–19352.
- [12] W.Z. Wang, X.W. Huang, S. Wu, Y.X. Zhou, L.J. Wang, H.L. Shi, Y.J. Liang, B. Zou, *Appl. Catal. B: Environ.* 134 (2013) 293–301.
- [13] S.F. Chen, Y.F. Hu, S.M. Meng, X.L. Fu, *Appl. Catal. B: Environ.* 150 (2014) 564–573.
- [14] Y.Z. Hong, Y.H. Jiang, C.S. Li, W.Q. Fan, X. Yan, M. Yan, W.D. Shi, *Appl. Catal. B: Environ.* 180 (2016) 663–673.
- [15] Y. Zheng, L.H. Lin, X.G. Ye, F.S. Guo, X.C. Wang, *Angew. Chem. Int. Ed.* 53 (2014) 11926–11930.
- [16] J.S. Zhang, M.W. Zhang, L.H. Lin, X.C. Wang, *Angew. Chem. Int. Ed.* 54 (2015) 6297–6301.
- [17] G.G. Zhang, M.W. Zhang, X.X. Ye, X.Q. Qiu, S. Lin, X.C. Wang, *Adv. Mater.* 26 (2014) 805–809.
- [18] Y.J. Cui, Z.X. Ding, X.Z. Fu, X.C. Wang, *Angew. Chem. Int. Ed.* 51 (2012) 11814–11818.
- [19] J.S. Zhang, Y. Chen, X.C. Wang, *Energy Environ. Sci.* 8 (2015) 3092–3108.
- [20] M.W. Zhang, X.C. Wang, *Energy Environ. Sci.* 7 (2014) 1902–1906.
- [21] J.S. Zhang, M.W. Zhang, C. Yang, X.C. Wang, *Adv. Mater.* 26 (2014) 4121–4126.
- [22] Z.Z. Lin, X.C. Wang, *Angew. Chem. Int. Ed.* 52 (2013) 1735–1738.
- [23] G.G. Zhang, Z.A. Lan, L.H. Lin, S. Lin, X.C. Wang, *Chem. Sci.* 7 (2016) 3062–3066.
- [24] Y. Zheng, L.H. Lin, B. Wang, X.C. Wang, *Angew. Chem. Int. Ed.* 54 (2015) 12868–12884.
- [25] D.D. Zheng, X.N. Cao, X.C. Wang, *Angew. Chem. Int. Ed.* 55 (2016) 11512–11516.
- [26] C.C. Chen, W.H. Ma, J.C. Zhao, *Chem. Soc. Rev.* 39 (2010) 4206–4219.
- [27] H. Li, J. Shang, J.G. Shi, K. Zhao, L.Z. Zhang, *Nanoscale* 8 (2016) 1986–1993.
- [28] S.C. Jensen, S.B. Homan, E.A. Weiss, *J. Am. Chem. Soc.* 138 (2016) 1591–1600.
- [29] H. Sheng, H.W. Ji, W.H. Ma, C.C. Chen, J.C. Zhao, *Angew. Chem. Int. Ed.* 52 (2013) 9686–9690.
- [30] C.C. Chen, T. Shi, W. Chang, J.C. Zhao, *ChemCatChem* 7 (2015) 724–731.
- [31] W. Chang, C.Y. Sun, X.B. Pang, H. Sheng, Y. Li, H.W. Ji, W.J. Song, C.C. Chen, W.H. Ma, J.C. Zhao, *Angew. Chem. Int. Ed.* 54 (2015) 2052–2056.
- [32] H. Sheng, H.N. Zhang, W.J. Song, H.W. Ji, W.H. Ma, C.C. Chen, J.C. Zhao, *Angew. Chem. Int. Ed.* 54 (2015) 5905–5909.
- [33] V. Donchev, K. Kirilov, T. Ivanov, K. Germanova, *Mater. Sci. Eng. B-Solid* 129 (2006) 186–192.
- [34] L. Ge, F. Zuo, J.K. Liu, Q. Ma, C. Wang, D.Z. Sun, L. Bartels, P.Y. Feng, *J. Phys. Chem. C* 116 (2012) 13708–13714.
- [35] X.C. Wang, K. Maeda, A. Thomas, K. Takanabe, G. Xin, J.M. Carlsson, K. Domen, M. Antonietti, *Nat. Mater.* 8 (2009) 76–80.
- [36] P. Niu, G. Liu, H.M. Cheng, *J. Phys. Chem. C* 116 (2012) 11013–11018.
- [37] S.C. Yan, Z.S. Li, Z.G. Zou, *Langmuir* 26 (2010) 3894–3901.
- [38] X.F. Li, J. Zhang, L.H. Shen, Y.M. Ma, W.W. Lei, Q.L. Cui, G.T. Zou, *Appl. Phys. A: Mater. Sci. Process.* 94 (2009) 387–392.
- [39] Y.D. Guo, G.K. Zhang, H.H. Gan, Y.L. Zhang, *Dalton Trans.* 41 (2012) 12697–12703.
- [40] Z. Wan, G.K. Zhang, J.T. Wang, Y.L. Zhang, *RSC Adv.* 3 (2013) 19617–19623.
- [41] J. Liu, G.K. Zhang, J.C. Yu, Y.D. Guo, *Dalton Trans.* 42 (2013) 5092–5099.
- [42] L. Liu, D. Ma, H. Zheng, X.J. Li, M.J. Cheng, X.H. Bao, *Microporous Mesoporous Mater.* 110 (2008) 216–222.
- [43] X.D. Meng, G.K. Zhang, N. Li, *Chem. Eng. J.* 314 (2017) 249–256.
- [44] D.D. Tang, G.K. Zhang, *Appl. Surf. Sci.* 391 (2017) 415–422.
- [45] Z. Wan, G.K. Zhang, *J. Mater. Chem. A* 3 (2015) 16737–16745.
- [46] Y.F. Fang, Y. Zhang, W.H. Ma, D.M. Johnson, Y.P. Huang, *Appl. Catal. B: Environ.* 160–161 (2014) 597–605.
- [47] X.P. Huang, X.J. Hou, F.H. Song, J.C. Zhao, L.Z. Zhang, *Environ. Sci. Technol.* 50 (2016) 1964–1972.
- [48] M. Bhawmik, A. Maity, V.V. Srinivasu, M.S. Onyango, *J. Hazard. Mater.* 190 (2011) 381–390.
- [49] H. Wang, X.Z. Yuan, Y. Wu, G.G. Zeng, X.H. Chen, L.J. Leng, Z.B. Wu, L.B. Jiang, H. Li, *J. Hazard. Mater.* 286 (2015) 187–194.
- [50] H. Fida, S. Guo, G.K. Zhang, *J. Colloid Interface Sci.* 442 (2015) 30–38.
- [51] X. Zou, Z. Wan, C.Y. Wan, G.K. Zhang, X.J. Pan, J.H. Peng, J.J. Chang, *J. Mol. Catal. A: Chem.* 411 (2016) 364–371.
- [52] L. Chen, W.L. Chen, H.Q. Tan, J.S. Li, X.J. Sang, E.B. Wang, *J. Mater. Chem. A* 4 (2016) 4125–4133.
- [53] G. Sharm, Z.Q. Zhao, P. Sarker, B.A. Nail, J.R. Wang, M.N. Huda, F.E. Osterloh, *J. Mater. Chem. A* 4 (2016) 2936–2942.
- [54] D.D. Tang, G.K. Zhang, *Ultrason. Sonochem.* 37 (2017) 208–215.
- [55] D. Lu, G.K. Zhang, Z. Wan, *Appl. Surf. Sci.* 358 (2015) 223–230.
- [56] H.Y. Jiang, G.G. Liu, T. Wang, P. Li, J. Lin, J.H. Ye, *RSC Adv.* 5 (2015) 92963–92969.
- [57] C.M. Braun, A. Fujishima, *J. Appl. Phys.* 62 (1987) 2107–2110.